

Numerical Investigation of Ti6Al4V Gradient Lattice Structures with Tailored Mechanical Response

Daniel Camilo Mora Sierra, Asghar Heydari Astaraee, Mario Guagliano, and Sara Bagherifard*

Open porous lattice structures have found a wide range of applications as lightweight load-bearing and energy absorbent structures in various fields. A common requirement for any application is the preliminary assessment of the mechanical response of the proposed architecture. Herein, uniform and continuous functionally graded lattice structures (FGLSs) made of titanium alloy, Ti-6Al-4V, are designed using cubic and pillar octahedron unit cells at overall porosities of 60%, 75%, and 85%. The lattice morphology is modulated using axial, dense-in, and dense-out gradient strategies. The mechanical performance of the structures is studied using numerical simulations implementing damage initiation and evolution under quasi-static compression. The proposed models could properly simulate the mechanical properties and failure behavior of the lattice structures. The designed FGLSs displays a crushing behavior starting from the lower relative density layers toward the higher relative density ones. Cubic and pillar octahedron-based structures exhibit stretch- and bending-dominated deformation behaviors, respectively. The power-law analysis verified by the Gibson–Ashby model is used to assess the mechanical response of the FGLSs. The effect of the gradient strategies on the mechanical properties as well as their adaptability for orthopedic implants is discussed in detail.

of these intricate geometries. In fact, over 90% of metallic OPLSs are manufactured using a powder bed fusion (PBF) process.^[2] These structures have been utilized in lightweight and energy absorption applications in aerospace^[3,4] and automotive^[5,6] industries, as well as for body protection.^[7] OPLSs are also used in biomedical applications as bone implants matching the mechanical properties of the host tissue, and allowing cell migration and proliferation thanks to the interconnected porous structure, offering at the same time an increased exposed surface for better osseointegration.^[8,9]


No matter what is the practical aim of these materials, the load-bearing ability of OPLSs plays a crucial role before every application can be developed. Indeed, the mechanical properties, and thus the functionality of the OPLSs can be modified by adjusting structural parameters such as unit cell size, strut cross-sectional dimensions, and porosity.^[10–12] OPLS can be in the form of cellular structures with periodic unit cells of identical porosity, known as uniform lat-

tice structures (ULSs). In the opposite category, there exist functionally graded lattice structures (FGLSs) with a spatial variation in the internal architecture of the unit cell or material composition. FGLSs have the potential to provide an optimum internal architecture improving the overall mechanical properties. Cobalt-chromium FGLSs processed by laser PBF were manufactured using different strut size pillar octahedron unit cells with the gradient being along the radial and longitudinal direction.^[13] Elastic modulus, yield strength, and compressive strength of FGLSs were almost the same as that of the ULSs at equal relative density. However, larger yield and ultimate compressive strength were achieved in structures with radial density gradients compared to axial density gradients. The proposed FGLSs proved to be a probable solution to the common problem of stress shielding due to Young's modulus mismatch between the solid metallic implant and the natural bone. Maskery et al.^[14] manufactured FGLSs made of Al–Si10–Mg using PBF technology. They reported that FG structure avoided the common shear collapse in ULSs and the related large stress drop in the stress–strain curve. Instead, the compressive response of FGLSs exhibited a step-like behavior, which provided a more predictable deformation behavior including energy absorption. It is also been reported that FGLSs are advantageous in biomedical applications.^[15,16] FGLSs are designed using diverse

1. Introduction

Open-porous lattice structures (OPLSs) are cellular solids fabricated by stacking periodically unit cells with specific geometrical features in the 3D space. OPLSs have more controllable architecture regarding cell size and wall thickness with respect to traditional porous cellular solids known as “foams”^[1] that are obtained by less controllable manufacturing processes. The advancement in additive manufacturing (AM) technologies has facilitated the realization

D. C. Mora Sierra, A. Heydari Astaraee, M. Guagliano, S. Bagherifard
Department of Mechanical Engineering
Politecnico di Milano
20156 Milan, Italy
E-mail: sara.bagherifard@polimi.it

 The ORCID identification number(s) for the author(s) of this article can be found under <https://doi.org/10.1002/adem.202101760>.

© 2022 The Authors. Advanced Engineering Materials published by Wiley-VCH GmbH. This is an open access article under the terms of the Creative Commons Attribution-NonCommercial-NoDerivs License, which permits use and distribution in any medium, provided the original work is properly cited, the use is non-commercial and no modifications or adaptations are made.

DOI: 10.1002/adem.202101760

approaches^[16–18]: 1) variation in strut diameter while keeping a constant unit cell size. Using this approach, the pore size and porosity can be incrementally graded layer-wise; 2) variation of unit cell size, which allows both strut and pore size modification. This approach is not always practical, because of the free nodes at the boundary between unit cells of different volumes, which induce the risk to decrease the mechanical performance of the FGLS; 3) assembling dissimilar unit cells. An extensive variety of possibilities are made available for FGLSs using the latter strategy providing the means to tune separately the geometric parameters, such as porosity, pore size, and strut diameter; 4) considering a mixture of at least two materials in the gradual transition.

Finite element (FE) modeling has extensively been applied in the analysis of cellular solids in general, and more specifically of OPLSs in the primary steps of the design process.^[19] Different FE modeling approaches are found in the literature. One category divides the models into infinite media models and finite-size models.^[20] The infinite media models consider only a single unit cell and make use of periodic boundary conditions with the advantage of a low computational cost. However, they lack the ability to study features such as deformation localization and structural irregularities.^[21] The finite size approach refers to stacking the unit cell in the 3D space and thus not applying periodic boundary conditions and thus is computationally more expensive. In this case, it is necessary to carefully choose the total number of unit cells to be considered to minimize the cell size effect. Regarding the type of FE model, solid or beam elements have been used in the literature. The former is computationally expensive but more suitable for plastic deformation and more able to consider local effects. The size effect is caused by the effect of boundary conditions and refers to the dependence of mechanical properties of lattice structures on the ratio of the specimen size to the cell size.^[22,23] In a numerical study by Smith et al.,^[24] it was demonstrated that the fundamental mechanical properties of the lattice structures can be predicted by a limited number of unit cells. Other studies such as Yang et al.^[25] and Kadkhodapour et al.^[26] have proven that lattice structures of $5 \times 5 \times 5$ unit cells can be safely used.

The high potential of gradient OPLSs to tune the mechanical properties has attracted considerable attention. However, the development of new structures is restricted by the limitations arising from the high expenses of fabrication as well as the costs and time required for their mechanical assessment. By the implementation of numerical modeling, these issues would be overcome more straightforwardly. In this study, a series of gradient OPLS is designed using cubic and pillar octahedron unit cells with three different gradient strategies of axial, dense-in, and dense-out. A numerical approach is utilized in the design procedure and FE analysis is implemented to investigate the quasi-static compressive mechanical behavior of the designed lattice structures to provide guidance for structural optimization at reduced costs. Hereafter, a finite-size solid FE model is developed to predict the mechanical properties and deformation mechanisms of the proposed FGLSs. The main compressive mechanical properties, including Young's modulus, peak stress, plateau stress, and energy absorption are compared. The collapse behavior as well as the power-law analysis of the structures are discussed.

2. Experimental Section

2.1. Structural Arrangements

Two types of unit cells having a cell size L of 2 mm were considered as the building unit of the FGLSs as shown in **Figure 1**. The first one is a cubic unit cell (C) architecture consisting of struts directed at 0 and 90 with respect to the compression direction (vertically) and having a quarter-circle cross-section (Figure 1a). The second is the pillar octahedron (Po) architecture. It consists of struts having both a quarter-circle cross-section directed at 0 in relation to the compression direction and a circular cross-section inclined at ± 45 with respect to the loading direction (Figure 1b).

The CAD model of the structures was built using Autodesk Inventor Professional 2019. The structures were $5 \times 5 \times 5$ unit cells with overall porosities of 60%, 75%, and 85%. The porosity, P , was calculated according to the following relation

$$P(\%) = 100 \frac{V_{\text{void}}}{V_{\text{tot}}} = 100 \frac{V_{\text{tot}} - V_{\text{solid}}}{V_{\text{tot}}} = 100 \left(1 - \frac{V_{\text{solid}}}{V_{\text{tot}}} \right) \quad (1)$$

where V_{tot} is the volume of the box enclosing the unit cell (L^3), V_{void} is the void volume within the enclosing box, and V_{solid} is the volume of the struts, obtained from the CAD models.

Three different gradient strategies were utilized, namely axial gradient (Ax), dense-in gradient (Din), and dense-out gradient (Dout) (**Figure 2**). In all cases, the gradients consisted of a continuous linear change in strut diameter (D_{strct}) along the vertical axis of the structures, while keeping a constant unit cell geometry and unit cell size. The gradients were controlled by the values of two design-driving strut diameters specified at two different points in the structure. Ax is a variation of strut diameter from a maximum diameter, D_{max} , at the bottom of the structure to a minimum diameter, D_{min} , at the top of the structure (Figure 2a,d). Din is a strut variation from D_{min} at both the bottom and top of the structure to D_{max} in the middle layer (third layer bottom-up) of the structure (Figure 2b,e); D_{max} was kept constant to avoid a sharp corner right at the middle of the transient layer and the possible stress concentrations. Dout is the opposite of Din; the strut changes from D_{max} at both the bottom and top of the structure to D_{min} , which was kept constant in the middle layer of the structure as well (Figure 2c,f). In the case of cubic-based FGLSs, D_{min} and D_{max} were given to the vertical struts in the structure, while the horizontal ones have a diameter equal to that of the vertical struts at their corresponding vertical position. In contrast, D_{min} and D_{max} were specified on both vertical and ± 45 inclined struts on the pillar octahedron-based FGLSs. Uniform lattice structures (Uni) having the same overall porosities, 60%, 75%, and 85%, and building unit cell architectures and sizes were created as well. In that case, only one diameter, $D_{\text{min}} = D_{\text{max}}$, was used as the design-driving parameter to create the structure. The used labeling system is shown in **Table 1**. Diameters considered for each structure designed are provided in the supplementary, Table S1 and S2, Supporting Information, for both cubic- and pillar octahedron-based OPLSs, respectively.

The architectures of both unit cells allowed having fully interconnected highly porous lattice structures, which is an important requisite for cell migration and proliferation, as well as

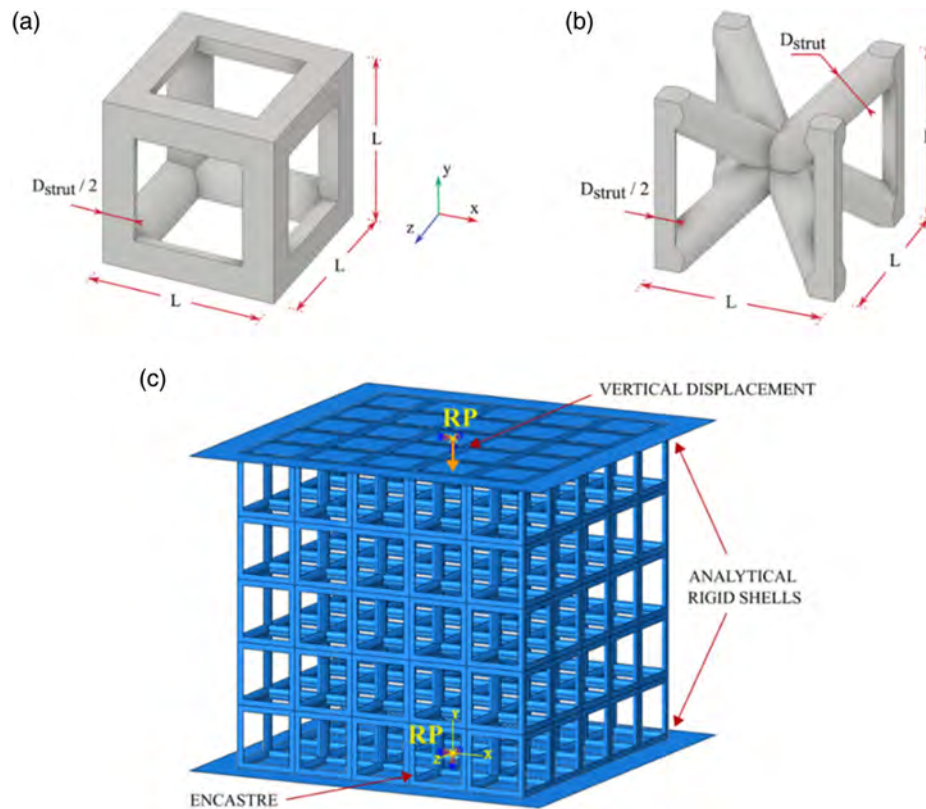


Figure 1. CAD model of: a) cubic and b) pillar octahedron unit cells. c) FEA model assembly and boundary conditions ($L = 2$ mm).

nutrient-waste flow transportation for biomedical applications.^[9] Pore size was defined as the largest inscribed circle corresponding to the 2D projection of the biggest sphere that can move in-between adjacent unit cells in a lattice structure.^[19,27–30] In the case of cubic-based lattice structures, given the architecture of the unit cell, only one pore type was defined (Figure 2g). In contrast, two different pore types were defined for the pillar octahedron-based lattice structures; intra-cell pore type, which is given by the unit cell morphology itself, and inter-cell pore type, which is the one generated when unit cells are stuck together (Figure 2h). Considering both uniform and graded structures, the pore size ranged from 860 to 1522 μm for cubic-based lattice structures, while pillar octahedron intra-cell and inter-cell pore size ranged from 335 to 765 μm and 729 to 1134 μm , respectively.

2.2. Numerical Modeling

A FE model was developed to estimate the mechanical properties and deformation mechanisms of OPLSs subjected to uniaxial quasi-static compression. The commercial software package ABAQUS/explicit 2017 was used to create the 3D explicit model. Lattice structures made of $5 \times 5 \times 5$ unit cells repeated along the 3 global coordinates and having a unit cell size (L) equal to 2 mm, were considered. Details of the numerical model are shown in Figure 1c. Two analytical rigid shells were created to replicate the upper and lower compression plates of the testing machine. All degrees of freedom were blocked for

the bottom plate, while the upper one was only allowed to have a displacement in the vertical direction to compress the structure by 50% of its initial height (Figure 2c). The reference point located on the upper plate was used to extract the displacement and reaction force from the structure, which is then converted into the corresponding engineering stress–strain curve. Ten-node modified quadratic tetrahedral elements, C3D10M, were used to mesh the OPLSs. To optimize the accuracy of the results as well as the computational cost, a mesh convergence study was carried out leading to an element size of 0.14 mm. The total number of elements for each unit cell type is provided in the supplementary data in Table S1 and S2, Supporting Information. A contact algorithm was implemented to consider all the possible interactions including with-self ones in the simulation. Contact properties were enforced with the penalty method taken as tangential behavior with a coefficient of friction of 0.2.^[31]

Material properties were defined in such a way to implement the failure initiation and model the progressive damage and failure of the OPLSs. The elastic modulus was set to 110 GPa and Poisson ratio to 0.3. Plasticity data were obtained from^[32,33] corresponding to annealed LPBF Ti6Al4V built in the vertical direction.

Damage was modeled using the Johnson–Cook damage initiation criterion, which is a strain-based fracture model proposed.^[34] It states that the equivalent plastic strain at the onset of damage, $\bar{\epsilon}_0^{\text{pl}}$, is usually dependent on the stress triaxiality, the strain rate, and the temperature

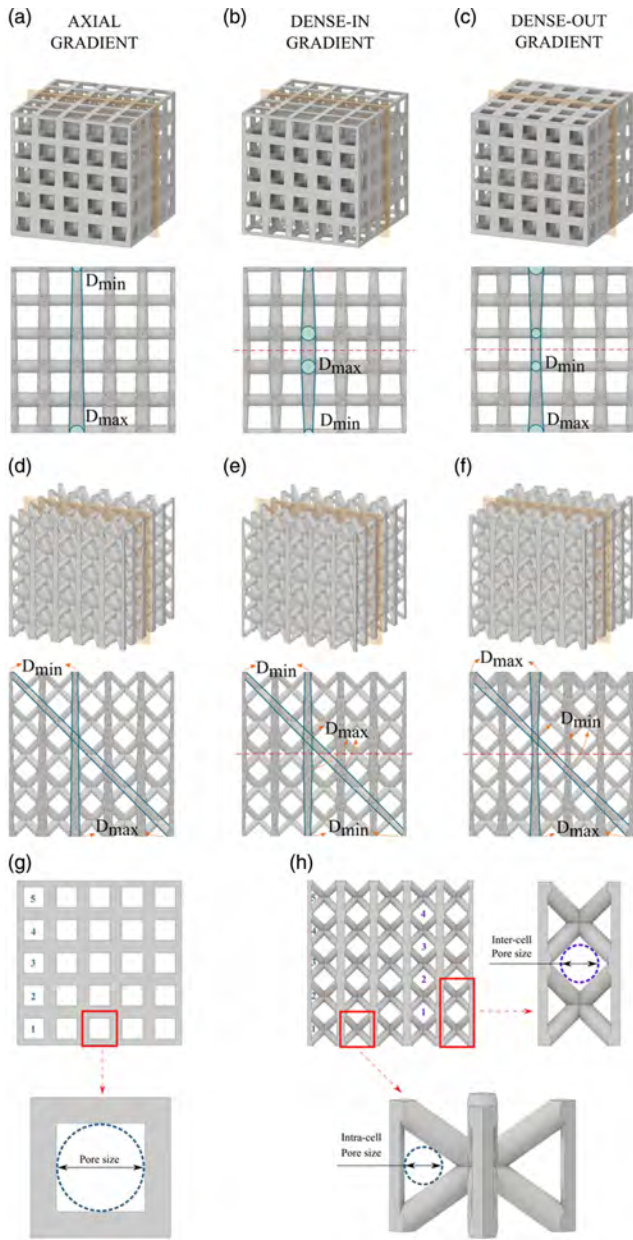


Figure 2. CAD models and section view of FGLS of 75% porosity based on both: a–c) cubic and d–f) pillar octahedron unit cell, and having axial (a,d), dense-in (b,e), and dense-out (c,f) structural gradients; definition of: g) cubic unit cell pore size, and h) pillar octahedron intra-cell and inter-cell pore size.

$$\bar{\epsilon}_0^{pl} = [D_1 + D_2 \exp(D_3 \sigma^*)][1 + D_4 \ln(\dot{\epsilon}^*)][1 + D_5 T^*] \quad (2)$$

where σ^* is the stress triaxiality, T^* is the homologous temperature, $\dot{\epsilon}^*$ is the dimensionless strain rate, and D_1 to D_5 are material constants. The five material constants used for Ti6Al4V are listed in **Table 2**.^[26] Constants D_4 and D_5 were set to zero since the compression tests were carried out under quasi-static conditions at room temperature.

Table 1. Labeling of the various structural arrangements.

Porosity (%)	Uniform	Axial	Dense-in	Dense-out
Cubic unit cell				
60	C-Uni60	C-Ax60	C-Din60	C-Dout60
75	C-Uni75	C-Ax75	C-Din60	C-Dout75
85	C-Uni85	C-Ax85	C-Din60	C-Dout85
Pillar octahedron unit cell				
60	Po-Uni60	Po-Ax60	Po-Din60	Po-Dout60
75	Po-Uni75	Po-Ax75	Po-Din60	Po-Dout75
85	Po-Uni85	Po-Ax85	Po-Din60	Po-Dout85

Table 2. Johnson–Cook damage criterion material constants for Ti6Al4V.^[26]

D1	D2	D3	D4	D5
−0.68	0.73	−0.25	0	0

The damage evolution law describes the behavior of the material after damage initiation. That is, the progressive degradation of the material's stiffness once the damage initiation criterion is fulfilled. Damage evolution was specified in terms of the fracture energy per unit area, G_f , to be dissipated during the damage process. The value of G_f was calculated using the fracture mechanics expression (Equation (3)), which is a function of the fracture toughness K_{Ic} , Young's modulus E , and Poisson's ratio ν , as follows.^[35,36]

$$(G_f)_I = \left(\frac{1 - \nu^2}{E} \right) (K_{Ic}^2) \quad (3)$$

The numerical value of K_{Ic} ^[32] and the calculated value of G_f are given in **Table 3**.

One crucial factor in the FE simulation is the computational cost. Time scaling and mass scaling are two approaches normally used to reduce computational time. The former means to speed up the analysis as opposed to the event's natural time scale and can be used only in the cases where rate-dependent material properties are not used. The latter means to artificially increase the density of the material, which in consequence decreases the wave speed propagation through an element, and finally increases the stable time increment of the analysis, making the simulation run faster. In this study, time scaling, rather than mass scaling, was applied, considering a compressive velocity of 6 m s^{-1} . This velocity was selected based on some preliminary trials. Two criteria were considered: 1) the kinetic energy was monitored so as to make sure it did not exceed 10% of the

Table 3. Annealed LPBF Ti6Al4V material properties.^[26,32,33]

Elastic modulus (GPa)	Yield strength (MPa)	Density [g cm^{-3}]	Poisson's ratio	Fracture toughness [$\text{MPa } \sqrt{\text{m}}$]	G_f [m]
110	957	4.42	0.3	49 ± 2	21.517

internal energy throughout the process^[37,38] and 2) the compressive force-displacement had to be independent of the applied velocity.^[38]

2.3. Mechanical Properties

Mechanical properties were estimated from the results of the numerical simulations and following the standards ISO 13 314:2011.^[39] The yield stress was computed as the intersection between the compressive stress-strain curve and the 0.2% offset line parallel to the elastic region. The peak stress was estimated as the compressive stress corresponding to the first local maximum in the stress-strain curve. In the case of the plateau stress, the standard^[39] suggests two ways to calculate it, depending on the plateau end strain. First, as the arithmetical mean of stresses within the strain interval 20–30%, and second, as the arithmetical mean of stresses within the strain interval 20–40%. Since the OPLSs were not compressed all the way to be able to identify the densification stage in the stress-strain curve for all the cases, the plateau end strain could not be properly identified. Therefore, the plateau stress was calculated in both manners. Note that the value calculated considering the strain interval 20–30% is here denoted plateau03, while the one calculated considering the strain interval 20–40% is denoted as plateau04. The energy absorption per unit volume, W , was calculated according to the ISO 13 314:2011^[39] as

$$W = \frac{1}{100} \int_0^{e_0} \bar{\sigma} d\bar{\epsilon} \quad (4)$$

where e_0 is the upper limit of the compressive strain in percentage, which is the compressive strain 50%. The elastic modulus was obtained as the slope of the straight line given by linear fitting of data points within the linear deformation region at the beginning of the compressive stress-strain curve. To enhance the accuracy of these calculations, in addition to the simulations at 6 m s^{-1} displacement rate, another set of simulations was performed for each structure at 1 m s^{-1} only considering the corresponding elastic regime. Furthermore, the data point acquisition rate was increased.

3. Results and Discussion

Validity of the developed numerical model was verified by comparing the results obtained from analysis on lattice structures having a cubic unit cell morphology, and the experimental data available in the literature^[26] by applying the same unit cell geometry and testing conditions in the numerical model. The numerical and experimental compressive stress-strain curves at an identical relative density showed a very good match (Figure S1, Supporting Information). Such comparison led to the conclusion that the numerical model including the damage initiation and damage evolution is able to properly predict the mechanical characteristics of the OPLSs.

Stress-strain curves of cubic and pillar octahedron-based lattice structures are presented in **Figure 3**. Every curve displays the typical trend of cellular materials, given by a linear elastic region, followed by an energy absorption plateau regime, and ending

with a densification stage, although the latter is not evident because the structure was not compressed up to such values of strain. Uniform lattice structures, regardless of the constituent unit cell and porosity, show a post-yield strain-softening behavior (Figure 3a,e). It means that prior to the densification regime, the values of stress do not reach back to the peak stress initially registered. In contrast, FGLSs display different behavior, i.e., post-yield strain hardening (Figure 3b–d,f–h). Even though an evident post-yield stress drop happens in every case, stress values higher than the peak stress are reached as the compression proceeds in the plateau regime. The only exception happens for C-Dout85 FGLS; in this case, although stress values do not reach higher than the initial peak stress, equivalent values are obtained (Figure 3d). Cubic-based OPLSs have large stress fluctuations in the plateau regime, while pillar octahedron-based lattice structures show low-amplitude stress variations, representing a more uniform plateau region. This can be explained by the architecture of the constituent unit cells and so the nature of deformation. In contrast, strut orientation in a cubic-based lattice structure is both parallel and perpendicular to the loading direction, which implies that the cubic topology generates stretch-dominated structures.^[26] In contrast, pillar octahedron-based lattice structures have struts both parallel and inclined at $\pm 45^\circ$ with respect to the loading direction. According to different studies in the literature, pillar octahedron topology shows a stretch-dominated behavior due to the struts aligned with the loading direction^[40–42]; nevertheless, in this study, such unit cell topology was seen to have a behavior in between the stretch and bending-dominated, although tending towards the bending-dominated one.

3.1. Collapse Behavior

Stress-strain curves are correlated to the damage evolution in the lattice structures, i.e., the deformation behavior. The layers are numbered from 5 to 1, top-down, for easier identification in this discussion. The deformation behaviors were displayed in figures only for representative cases (**Figure 4**). The results indicate that the collapse of cubic FGLSs is always initiated from the layers with the lowest relative density towards the layer with the highest density. That is the reason why the corresponding stress-strain curves show higher peak stresses as the strain increases. Additionally, the number of collapsed layers varied depending on the porosity of the structures. The higher the relative density, the lower the pore size; hence, lattice structures with higher overall relative density may have more layers fully densified since lower compressive displacement is needed to compress individual layers. Regarding C-Ax structures, the collapse went from the top layer toward the one at the bottom (Figure 4a). C-Ax60 was fully compressed down to the second layer, while C-Ax75 and C-Ax85 were compressed down to the third layer. Deformation in C-Din structures always started from the first layer, followed by the fifth, and then both the fourth and the second layer or either one depending on the structure (Figure 4b). However, C-Din75 had both the first and fifth layers compressed simultaneously. C-Dout60 was compressed in the order third layer, then fourth and second layer simultaneously, followed by the first layer (Figure 4c). C-Dout75 and C-Dout85

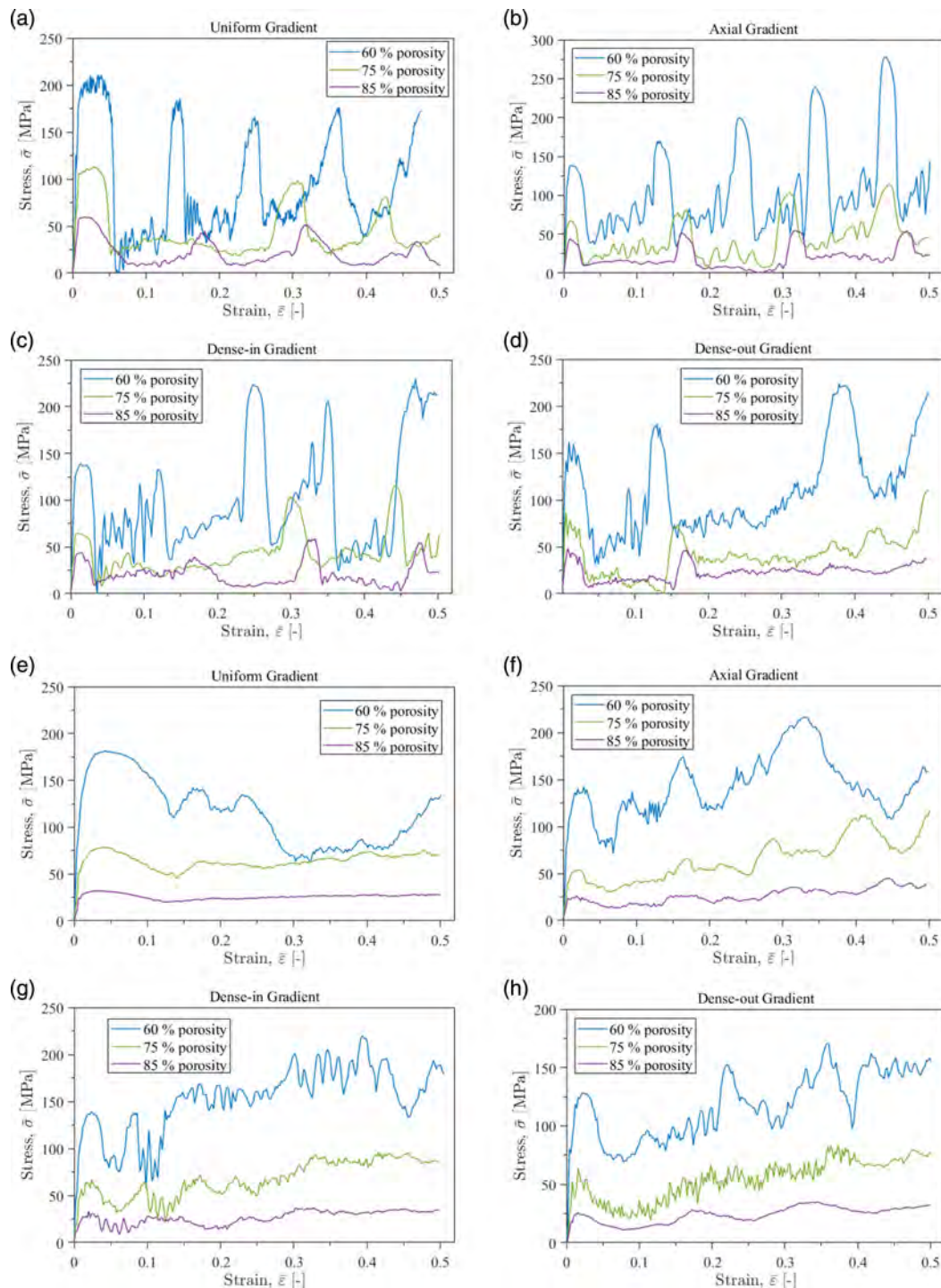


Figure 3. Stress–strain curves of: a) uniform, b) axially graded, c) dense-in graded, and d) dense-out graded cubic-based OPLSs; and e) uniform, f) axially graded, g) dense-in graded, and h) dense-out graded pillar octahedron-based OPLSs.

structures followed the same order, excluding the compression of the first layer, and the overall behavior of these structures was different compared to that of C-Dout60. On one hand, a shear band seemed to form in C-Dout60 when the fourth and second layers were compressed simultaneously, and the struts were

always vertically aligned. On the other hand, due to a lower relative density, the third layer in C-Dout75 and C-Dout85 was not capable of holding the struts aligned vertically and it seemed to buckle as it was compressed, leading to the vertical misalignment of fifth and fourth layers with respect to the first and second

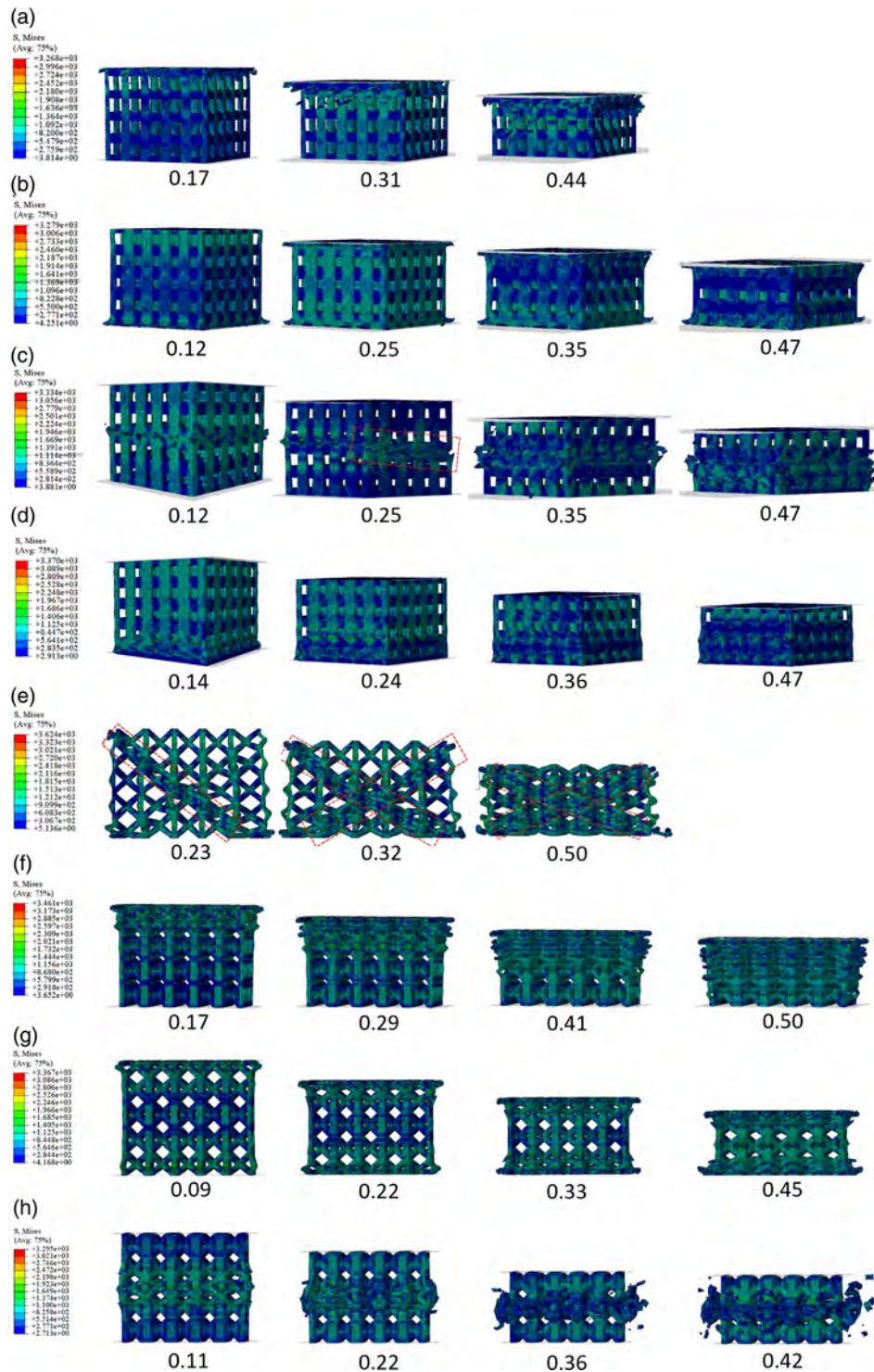


Figure 4. Deformation behavior and damage evolution during compression of: a) C-Ax75, b) C-Din60, c) C-Dout60, d) C-Uni60, e) Po-Uni85, f) Po-Ax75, g) Po-Din75, and h) Po-Dout60. The values below each deformation stage indicate the total strain.

layers. Contrary to the case of cubic FGLSs, uniform structures did not exhibit any specific pattern regarding the deformation behavior. The C-Uni60 structure was compressed in the order first, second, third, and the fourth layer (Figure 4d). C-Uni85

followed the same pattern with the difference that the fourth layer did not reach full compression. C-Uni75 had a different deformation behavior; it started with the simultaneous compression of the fourth and third layers, followed by the second layer.

Overall, layer-by-layer collapse was observed in both C-Uni and C-FG structures. It means that as the compression went on, the deformation was mostly concentrated in a single layer, and only when the corresponding layer was fully compressed another layer started to collapse. Additionally, it was observed that full densification of either a single layer or in two, was reflected by a prominent peak in the stress–strain curves.

Po-Uni structures, in contrast, did not deform in a layer-by-layer manner. The structural collapse happened due to shear bands at $\pm 45^\circ$ with respect to the loading direction (Figure 4e). As the porosity increased, the shear bands were less visible. Po-FG structures (Figure 4f–h), like C-FG structures, collapsed starting from the layers with the highest porosity towards the layers with the lowest porosity. Nevertheless, the progress of deformation was not layer-by-layer due to the constituent unit cell topology. Instead, the deformation was localized in one half of a layer and once the half was flattened, deformation concentrated in the one half of another layer. Consequently, the structural collapse is less abrupt, and the peak stress magnitude is lower. Except for the Po-Ax structures, it becomes more complex to identify in the stress–strain curve, which peaks correspond to a compressed half layer. Furthermore, the structures show a more compliant behavior. Po-Ax structures were always compressed from the fifth layer down to one half of the second layer, regardless of the overall porosity (Figure 4f). Po-Din structures were compressed from both top and bottom layers (fifth and sixth layers) toward the middle one (third layer) in an alternating manner (Figure 4g). Po-Dout structures were compressed from the middle layer (third layer) toward both top and bottom layers (fifth and sixth layers) (Figure 4h).

3.2. Mechanical Properties

Mechanical properties of the cubic and pillar octahedron lattice structures are reported in **Tables 4** and **5** and are represented graphically in **Figures 5** and **6**, respectively. The results indicate a clear dependency of the mechanical properties of structures on porosity. All mechanical properties, regardless of the constituent unit cell, decrease as the overall porosity of the lattice structure increases. It means that OPLSs with lower overall porosities are stiffer, resist higher loads, and absorb more energy per unit volume.

Additionally, the mechanical properties show dependency on the constituent unit cell topology. For a specific gradient and overall porosity, the elastic modulus, yield stress, and peak stress are higher for cubic structures than those corresponding to Po structures. The only exception to this occurs with the structures C-Din60 and C-Din75, which have peak stresses lower by 0.1% and 4.2% than those of Po-Din60 and Po-Din75 structures, respectively. On the contrary, both values of plateau stress are higher for Po structures compared to cubic structures. Since the plateau regime is contributing the most to the energy absorption capabilities of an OPLS, the energy absorption per unit volume is higher in the case of Po structures. This corroborates the type of structures generated, i.e., bending-dominated and stretch-dominated. On one hand, cubic-based lattice structures present higher elastic modulus as well as initial collapse strength at a specific overall porosity, which is distinctive in stretch-dominated

Table 4. Mechanical properties of cubic-based lattice structures.

Label	Elastic modulus [GPa]	Yield stress [MPa]	Peak Stress [MPa]	Plateau 03 [MPa]	Plateau 04 [MPa]	Energy absorption [mJ mm ⁻³]
C-Uni60	23.0	189.5	210.9	82.6	91.0	44.0
C-Uni75	12.5	105.8	113.1	38.4	39.6	21.6
C-Uni85	7.02	58.4	59.5	14.4	19.9	11.1
C-Ax60	22.7	135.4	138.8	102.5	111.7	53.5
C-Ax75	12.1	68.6	67.3	25.2	39.0	21.4
C-Ax85	6.8	43.3	44.1	5.4	16.4	9.8
C-Din60	22.1	133.1	139.2	115.5	105.7	50.5
C-Din75	11.4	62.8	64.4	47.8	48.6	21.7
C-Din85	6.8	43.9	43.9	10.4	17.7	10.4
C-Dout60	22.7	145.2	162.2	80.7	115.7	55.3
C-Dout75	11.9	70.6	86.8	37.2	39.6	20.3
C-Dout85	6.7	43.6	48.0	22.5	23.9	11.4

Table 5. Mechanical properties of pillar octahedron-based lattice structures.

Label	Elastic modulus [GPa]	Yield stress [MPa]	Peak Stress [MPa]	Plateau 03 [MPa]	Plateau 04 [MPa]	Energy absorption [mJ mm ⁻³]
Po-Uni60	16.8	130.9	181.4	108.1	91.9	57.8
Po-Uni75	7.6	58.5	78.3	59.2	62.6	31.9
Po-Uni85	3.62	27.2	31.9	24.3	25.4	12.8
Po-Ax60	16.0	109.9	142.2	152.2	168.1	70.9
Po-Ax75	7.0	44.5	53.8	63.3	71.1	32.3
Po-Ax85	3.4	21.6	26.0	24.0	27.7	13.1
Po-Din60	15.7	110.3	139.4	161.2	173.7	76.9
Po-Din75	7.1	48.7	67.2	62.6	73.9	33.5
Po-Din85	3.4	21.6	33.5	24.5	28.9	13.2
Po-Dout60	15.1	100.8	128.3	119.3	127.7	59.0
Po-Dout75	6.5	40.5	64.0	56.4	62.0	27.1
Po-Dout85	3.2	20.3	25.9	22.7	27.1	11.9

structures and makes them ideal for lightweight loadbearing applications.^[43] Po structures, on the other hand, seem to be more compliant and show a plateau regime with a lower amplitude of stress fluctuations as well as higher energy absorption per unit volume at a specific overall porosity. All these considered, the latter tend to the behavior of bending-dominated structures, which are desirable for energy-absorbing applications.^[43]

The change from Uni into FG structures also affects the mechanical properties. Overall, the elastic modulus remains equivalent regardless of the porosity and constituent unit cell. There is a clear increase in energy absorption per unit volume at 60% porosity. However, at both 75% and 85%, the values remain comparable. Maskery et al.^[14] assessed the mechanical response of graded and uniform AlSi10Mg lattice structures fabricated by PBF. They used a density-based gradient strategy by a linear change of strut size, with the higher relative density at the

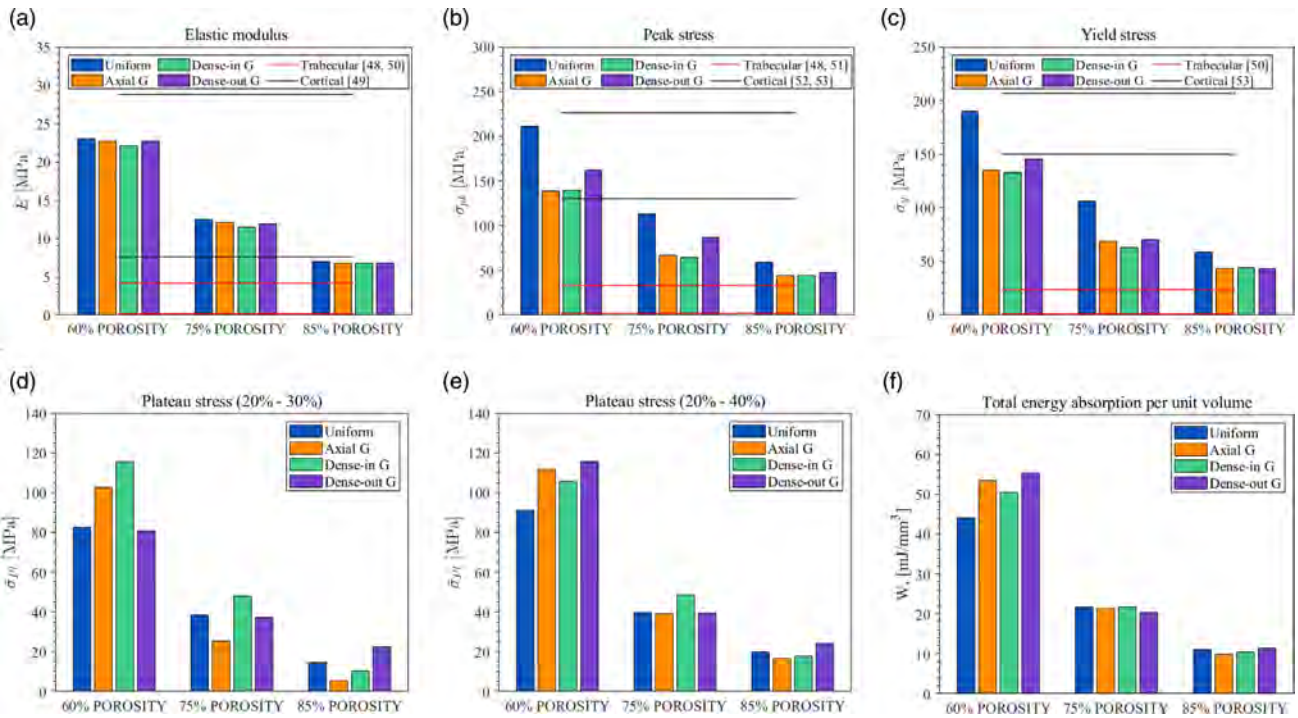


Figure 5. Bar graphs representing the mechanical properties numerically obtained for cubic-based lattice structures (the pairs of horizontal lines in (a–c) indicate the range of the corresponding mechanical property for trabecular and cortical human bone).

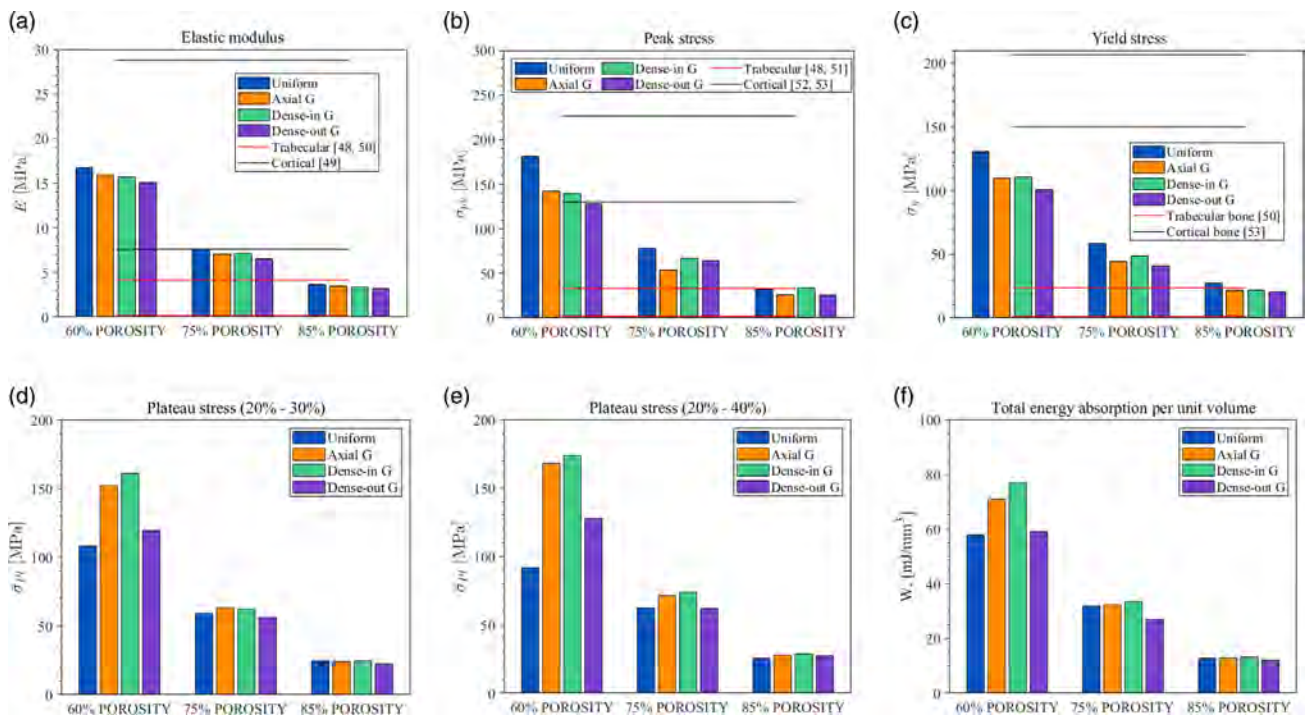


Figure 6. Bar graphs representing the mechanical properties numerically obtained for pillar octahedron-based lattice structures (the pairs of horizontal lines in (a–c) indicate the range of the relevant mechanical property for trabecular and cortical human bone).

base. Similar to our findings, their results showed approximately the same level of energy absorption capacity for the uniform and graded structures. The peak stress decreases at all porosities and

the trends vary depending on the constituent unit cell. In the case of cubic OPLSs, the gradient giving the highest peak stress is always the Dout, while the values for both Ax and Din are always

equivalent. On the contrary, Po structures do not show a regular trend. At 60%, the highest peak stress corresponds to the Po-Ax structure, while at both 75% and 85%, it corresponds to the Po-Din. The yield stress decreases at all porosities and the trends vary depending on the constituent unit cell. At both 60% and 85%, the lowest and highest yield stresses are given by C-Din and C-Dout, respectively. At 85%, all gradients give equivalent values of yield stress. Po structures have comparable values of yield stress for the Ax and Din gradients at both 60% and 85%, while Dout gradient provides the lowest value. At 75% porosity, the lowest and highest yield corresponds to Dout and Din gradients, respectively. The values of plateau stress of Po structures tend to be higher for all the gradients, with a bigger increase at 60% porosity. In the case of cubic structures only at 60%, the values of plateau tend to be higher. At 75% and 85%, there is always a bigger value for Din and Dout gradients, respectively.

The mechanical and biological functioning of bone scaffolds is highly dependent on the internal architecture of the unit cell. Previous studies have shown that ULSs can be manufactured with mechanical properties very similar to the ones of the bone with also proper biological characteristics for cell migration and proliferation.^[13,15,44–46] However, the direction in novel advances in tissue engineering is toward designing FGLSs that can better mimic the complex architecture of bone tissue.^[8,18] For this reason, the results of the proposed structures are discussed for biomedical applications. The values of elastic modulus, yield stress, and peak stress were compared to those of human trabecular and cortical-bone-derived from,^[47–53] as shown in Figures 5 and 6. The most important mechanical property to be considered is the elastic modulus since it dictates whether stress shielding happens or not especially when an orthopedic implant is used.^[13,16] The elastic modulus of all cubic structures at both 60% and 75% were within the range of the values for human cortical bone. Po structures at 60% porosity were within the range of elastic modulus of cortical bone, while at 85% the values were within the range of trabecular bone. Peak stresses of both cubic and Po structures at 60% porosity were within the range of values of compressive strength of cortical bone. At 85% porosity, the values of peak stress were within the range of trabecular bone only for Po structures. Regarding the yield stress, only the C-Uni60 structure was within the range of cortical bone. Only at 85% porosity, the Po structures were within the range of trabecular bone.

3.3. Mechanical Properties-Relative Density Relation Analysis

It is known that there exists a dependency of mechanical properties with the relative density of lattice structures, $\bar{\rho}/\rho_s$. Positive power-law relationships as in the Gibson–Ashby model can be used to represent such dependency.^[54] The general description of this relation is in the form

$$\frac{\bar{P}}{P_s} = C \left(\frac{\bar{\rho}}{\rho_s} \right)^\alpha \quad (5)$$

where \bar{P} is a property of the structure, P_s is the corresponding property of the base material the structures are made of, C is a proportionality constant and α is a fixed exponent. Equation (5)

was used to relate the numerical relative elastic modulus, \bar{E}/E_s , and relative yield strength $\bar{\sigma}_y/\sigma_{ys}$ to the relative density. Relative mechanical properties are obtained by normalizing the ones of the lattice structures, indicated by a macron symbol (horizontal line on top), with respect to the mechanical properties of the bulk material, indicated by the subscript “s”. Mechanical properties of the bulk material were indicated in Table 3. Proportionality coefficients, exponential coefficients, and coefficients of determination corresponding to the power fitting performed for different unit cell-based lattice structures are reported in Table 6. Overall, the coefficient of determination R^2 was higher than 0.994 and 0.97, for elastic modulus and yield strength, respectively, demonstrating a good fit.

The Gibson–Ashby model also evidences the dependency of mechanical properties of lattice structures on the type of response exhibited by the structure (bending- or stretch-dominated). Accordingly, the relative modulus and strength of bending-dominated lattice structures are respectively proportional to the square ($m = 2$) and the one and a half ($n = 1.5$) of the relative density, with a constant of proportionality C_1 .^[54] Concerning the stretched-dominated behavior, the relationship is linear for both mechanical properties ($m = n = 1$), with a constant of proportionality C_2 .^[43] Relative elastic modulus and strength of the lattice structures were fitted to the Gibson–Ashby model considering the ideal bending and stretched-dominated behaviors, and then compared to the fitted power laws previously discussed.

Since the obtained power trends for cubic structures were in good agreement with the one attributed to the structures with stretch-dominated behavior (exponential coefficients m and n close to 1), the mechanical properties of these structures could be fitted to the ideal stretch-dominated relation. On the contrary, the obtained power trends for Po structures are closer to the trend attributed to bending-dominated structures (exponential coefficients m and n approach to 2 and 1, respectively); therefore, these lattice structures were fitted to the ideal bending-dominated relation. The corresponding proportionality coefficients and the coefficients of determination are reported in Table 7. Log–log graphs are shown in Figure 7 to better visualize the behavior of the lattice structures. For the sake of brevity, only the ones corresponding to the relative elastic modulus and relative yield strength of Ax structures are displayed. The proportionality coefficient C_1 corresponding to the relative elastic

Table 6. Coefficients of power fitting analysis for mechanical properties of the reported lattice structures.

Label	\bar{E}/E_s			$\bar{\sigma}_y/\sigma_{ys}$		
	C_1	m	R^2	C_2	n	R^2
C-Uni	0.647	1.24	0.999	0.6	1.21	0.999
C-Ax	0.656	1.269	0.998	0.448	1.27	0.988
C-Din	0.65	1.286	0.995	0.45	1.3	0.971
C-Dout	0.67	1.293	0.997	0.517	1.35	0.988
Po-Uni	0.672	1.622	0.999	0.623	1.658	0.999
Po-Ax	0.664	1.662	0.997	0.594	1.8	0.996
Po-Din	0.628	1.621	0.999	0.546	1.7	0.999
Po-Dout	0.636	1.682	0.997	0.543	1.796	0.995

Table 7. Coefficients of Gibson–Ashby model obtained by fitting of reported lattice structures numerical data. Ideal S-d refers to ideal stretch dominated power fitting ($m = n = 1$), while ideal B-d refers to ideal bending dominated power fitting ($m = 2$ and $n = 1.5$).

Label	Predefined power law	\bar{E}/E_s			$\bar{\sigma}_y/\sigma_{ys}$		
		C_1	m	R^2	C_2	n	R^2
C-Uni	Ideal S-d	0.496	1	0.97	0.473	1	0.975
C-Ax		0.49	1	0.964	0.332	1	0.954
C-Din		0.472	1	0.957	0.322	1	0.931
C-Dout		0.484	1	0.958	0.35	1	0.938
Po-Uni	Ideal B-d	0.981	2	0.973	0.53	1.5	0.994
Po-Ax		0.932	2	0.978	0.436	1.5	0.979
Po-Din		0.92	2	0.973	0.444	1.5	0.991
Po-Dout		0.875	2	0.98	0.34	1.5	0.979

modulus was in the range 0.472–0.496 (decreased with respect to coefficients of power fitting reported in Table 6) and 0.875–0.981 (increased with respect to coefficients of power fitting reported in Table 6) for cubic and Po structures, respectively. Regarding the proportionality coefficient C_2 corresponding to the relative yield strength, the range was 0.322–0.473 (decreased with respect to coefficients of power fitting reported in Table 6) and 0.34–0.53 (decreased with respect to coefficients of power fitting reported in Table 6) for cubic and Po structures, respectively. Overall, considering both relative elastic modulus and strength, the power-law fit is good, although better in the case of Po structures ($R^2 > 0.972$) compared to cubic structures ($R^2 > 0.93$).

According to the Gibson–Ashby model, the proportionality coefficients C_1 and C_2 for metallic open-celled bending-dominated lattice structures fall in the range 0.1–0.4 and 0.1–1, respectively.^[55] However, the model does not pre-specify a range in the case of metallic open-celled stretch-dominated lattice structures. Nevertheless, a review study carried out by Alomar et al.^[20] collected the experimental data from the literature, and based on the lattice structures compressive behavior, identified a range for the proportionality constants for metallic

open-celled stretch-dominated structures of C1 and C2 to be in the range 0.02–0.3 and 0.1–0.6, respectively. In addition, they also identified the bending-dominated structures and determined a narrower and more precise range for the proportionality constants in comparison to the one proposed in the Gibson–Ashby model. The value C1 for metallic open-celled bending-dominated lattice structures was found to be in the range 0.1–0.6, while C2 was in the same range predicted in the Gibson–Ashby model. From the power-law fitting analysis (see Table 6), the coefficient of proportionality C2 estimated for both Po and cubic structures is within the ranges corresponding to bending- and stretch-dominated lattice structures, respectively. The coefficient of proportionality C1 for Po structures is within the range proposed by the Gibson–Ashby model for bending-dominated structures; however, it is out of the range established by Alomar et al.^[20] Likewise, C1 for cubic structures falls out of the range.

Log–log graphs comparing the power laws predicted for the different lattice structures to the proportionality constants ranges for both bending- and stretch-dominated metallic lattice structures are presented in **Figure 8**. The relative yield strength of cubic-based lattice structures is well predicted within the pre-specified boundaries of stretch-dominated structures. Likewise, the Po structures fall within the range pre-specified for bending-dominated structures. The relative elastic modulus of Po structures falls right in between the limits pre-specified by the Gibson–Ashby model for bending-dominated structures. On the contrary, it is outside the range established by Alomar et al.^[20] Similarly, the relative elastic modulus of cubic structures is outside of the range proposed by Alomar et al.^[20] One probable cause for this could be the fact that the proportionality constant ranges defined by Alomar et al.^[20] were obtained from experimental data rather than numerical simulation results. In this study, the modeling of lattice structures was performed considering the ideal CAD models. In reality, additively manufactured lattice structures have mechanical properties, especially the elastic modulus deteriorated due to different defects resulting from manufacturing, such as partially melted powder particles on the surface of as-built components, and residual thermal stresses, among others.^[25,56,57]

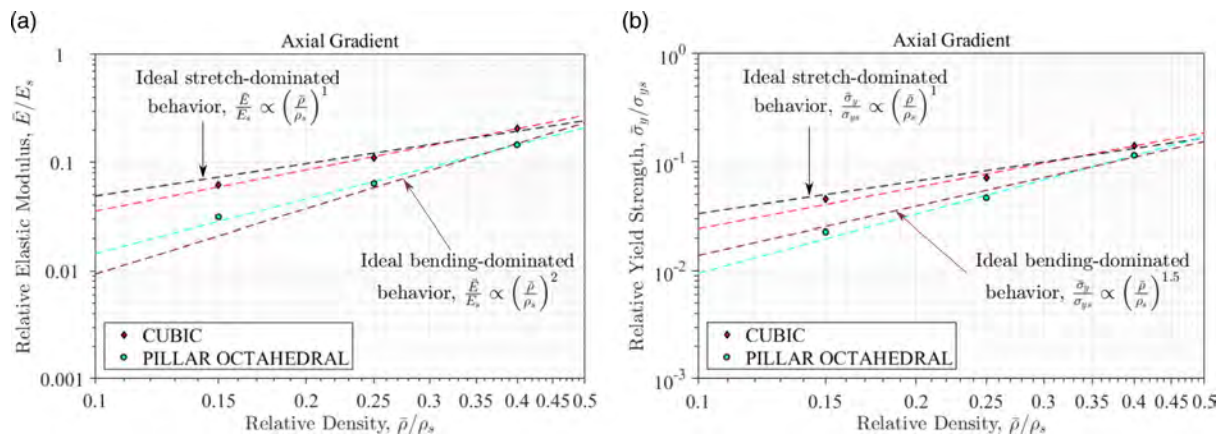


Figure 7. Log–log plots of power laws relating the: a) relative elastic modulus and b) relative yield strength of the reported axially graded lattice structures to the relative density, and a comparison with the Gibson–Ashby model fitting for ideal bending and stretch-dominated lattice structures.

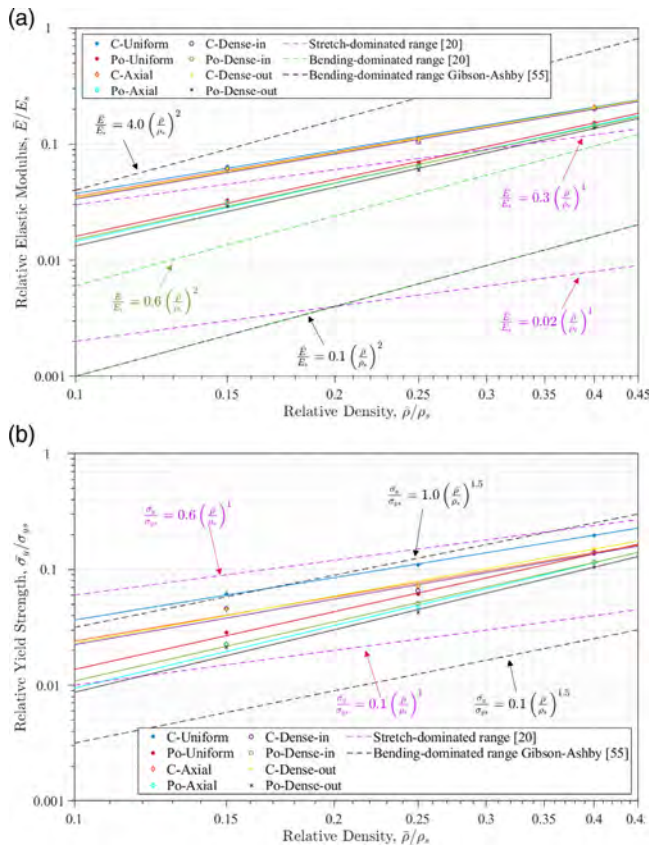


Figure 8. Log–log plots of power laws relating: a) the relative elastic modulus and b) the relative yield strength to the relative density of the reported lattice structures, and a comparison with the range for bending-dominated structures stated by the Gibson–Ashby model^[55] and Alomar et al.,^[20] and that for stretch-dominated structures stated by Alomar et al.^[20] Note that the legend “Bending dominated range” corresponds to the one stated by Alomar et al.^[20]

All things considered, power laws derived for the OPLSs show consistency with predictions of the Gibson–Ashby model. The variation of both relative elastic modulus and strength with the relative density follow closely the trend lines specified by the model. The power-law analysis is verified by the Gibson–Ashby model as a proper tool to obtain an initial estimation of mechanical properties of OPLSs having different constituent unit cell topologies.

Khadkhodapur et al.^[26] related the collapse behavior of the lattice structures to their dominant deformation mechanism. They found that stretch-dominated lattices show a layer-by-layer failure while bending-dominated lattices show failures in shear bands. In line with this, C-Uni and C-FG structures with a layer-by-layer failure and Po-Uni structures with diagonal shear bands failure (Section 3.1) were properly fitted to the stretch- and bending-dominated models, respectively. The lack of a shear band formation in FGLSs is previously reported due to gradient volume fraction throughout different layers.^[14,58] The Po-FG structures, in contrast, followed a half-layer alternating failure mechanism (Section 3.1), supposedly stemming from their graded nature, and depicted a good fit to the bending-dominated model, which was not reported previously in the literature.

4. Conclusions

In this work, Ti6Al4V LBPf-manufactured OPLS were numerically studied. Uniform, axially graded, dense-in graded, and dense-out graded OPLSs were suggested based on cubic and pillar octahedron unit cells at overall porosities of 60%, 75%, and 85%. A detailed numerical model was developed to predict the compressive mechanical behavior of the lattice structures. The influence of the design parameters was investigated on the mechanical performance and assessed for potential biomedical applications. The following conclusions are drawn:

The stress–strain curves of all the structures showed an elastic region, followed by a plateau regime. Contrary to the uniform structures, the functionally graded (FG) ones had a structural collapse always starting from the lower toward the higher relative density layers, regardless of the unit cell type.

The structural collapse showed dependency on the constituent unit cell. Both uniform and graded cubic-based lattice structures deformed always in a layer-wise manner. The uniform pillar octahedron-based lattice structures developed $\pm 45^\circ$ shear bands under compression, while the corresponding FG structures followed a half-layer alternating collapse.

Given a specific gradient and overall porosity, cubic-based structures displayed higher elastic modulus, peak stress, and yield stress, which makes them a better fit for lightweight load-bearing applications; pillar octahedron structures displayed higher plateau stress and energy absorption per unit volume, thus a better fit for energy absorbing applications.

The elastic modulus remained equivalent in all lattice structures having the same overall porosity and constituent unit cell. Both peak stress and yield stress decreased for FG structures with respect to uniform ones at all porosities. Plateau stress in pillar octahedron structures tended to be higher than that of uniform structures, at most of the porosities.

Upon comparison between the elastic modulus of the different considered structures and that of human cortical and trabecular bone, the most promising structures were identified for a potential biomedical application: Stress shielding in the cortical bone would be reduced or avoided for cubic lattice structures at 60% and 75% porosities, and pillar octahedron lattice structures at 60% porosity, regardless of the gradient. In the case of trabecular bone, among the studied designs, only the pillar octahedron lattice structures at 85% would be a good fit, independently from the gradient. Among the highlighted lattice structures, the choice would depend on the specific implantation site to define the range of the required mechanical properties and how they should vary throughout the structure.

The power-law analysis yielded a very good fit for both relative elastic modulus and relative yield strength. The fittings confirmed that cubic structures are stretch-dominated while pillar octahedron lattice structures showed a very good fit to bending-dominated structures.

The challenges associated with the fabrication of these structures could be related to the definition of the geometry, as some restrictions could be imposed by the minimum resolution. For PBF technique, which is the one commonly used for fabrication of lattice structures, it is generally $< 100 \mu\text{m}$. Another constraint may be imposed by the overhangs and the inclination of the features with respect to the build direction. There are specific

inclination angles set to guarantee the surface quality and integrity of the PBF build. Such aspects should be considered in the design for additive manufacturing (DfAM) phase to reduce issues during additive manufacturing of gradient OPLSs.

Supporting Information

Supporting Information is available from the Wiley Online Library or from the author.

Acknowledgements

Open Access Funding provided by Politecnico di Milano within the CRUI-CARE Agreement.

Conflict of Interest

The authors declare no conflict of interest.

Data Availability Statement

The data that support the findings of this study are available from the corresponding author upon reasonable request.

Keywords

additive manufacturing, AM, FGLS, gradient, lattice

Received: December 20, 2021

Revised: January 24, 2022

Published online: February 11, 2022

- [1] A. Heydari Astaraie, H. R. Shahverdi, S. H. Elahi, *Trans. Nonferrous Met. Soc. China* **2015**, 25, 162.
- [2] A. Nazir, K. M. Abate, A. Kumar, J.-Y. Jeng, *Int. J. Adv. Manuf. Technol.* **2019**, 104, 3489.
- [3] M. Bici, S. Brischetto, F. Campana, C. G. Ferro, C. Secli, S. Varetto, P. Maggiore, A. Mazza, *Procedia CIRP* **2018**, 67, 215.
- [4] S. K. Moon, Y. E. Tan, J. Hwang, Y.-J. Yoon, *Int. J. Precis. Eng. Manuf. Green Technol.* **2014**, 1, 223.
- [5] S. Yin, H. Chen, Y. Wu, Y. Li, J. Xu, *Compos. Struct.* **2018**, 201, 131.
- [6] K. J. Maloney, K. D. Fink, T. A. Schaedler, J. A. Kolodziejska, A. J. Jacobsen, C. S. Roper, *Int. J. Heat Mass Transfer* **2012**, 55, 2486.
- [7] J. Brennan-Craddock, D. Brackett, R. Wildman, R. Hague, *J. Phys. Conf. Ser.* **2012**, 382, 012042.
- [8] K. F. Leong, C. K. Chua, N. Sudarmadji, W. Y. Yeong, *J. Mech. Behav. Biomed. Mater.* **2008**, 1, 140.
- [9] D. W. Huttmacher, *Biomaterials* **2000**, 21, 2529.
- [10] A. Seharing, A. H. Azman, S. Abdullah, *Adv. Mech. Eng.* **2020**, 12, 1687814020916951.
- [11] R. Hedayati, A. M. Leeftang, A. A. Zadpoor, *Appl. Phys. Lett.* **2017**, 110, 091905.
- [12] L. Zhang, B. Song, L. Yang, Y. Shi, *Acta Biomater.* **2020**, 112, 298.
- [13] S. Limmahakhun, A. Oloyede, K. Sitthiseripratip, Y. Xiao, C. Yan, *Mater. Des.* **2017**, 114, 633.
- [14] I. Maskery, N. T. Aboulkhair, A. O. Aremu, C. J. Tuck, I. A. Ashcroft, R. D. Wildman, R. J. M. Hague, *Mater. Sci. Eng. A* **2016**, 670, 264.
- [15] E. Onal, J. E. Frith, M. Jurg, X. Wu, A. Molotnikov, *Metals* **2018**, 8, 200.
- [16] S. Limmahakhun, C. Yan, in *Scaffolds in Tissue Engineering: Materials, Technologies and Clinical Applications*, Croatia: IntechOpen, **2017**, pp. 75–94.
- [17] X.-Y. Zhang, G. Fang, L.-L. Xing, W. Liu, J. Zhou, *Mater. Design* **2018**, 157, 523.
- [18] G. H. Loh, E. Pei, D. Harrison, M. D. Monzón, *Addit. Manuf.* **2018**, 23, 34.
- [19] F. J. Quevedo González, N. Nuño, *Comput. Methods Biomech. Biomed. Eng.* **2016**, 19, 845.
- [20] Z. Alomar, F. Concli, *Adv. Eng. Mater.* **2020**, 22, 2000611.
- [21] M. R. Karamooz Ravari, M. Kadkhodaei, *J. Mater. Eng. Perform.* **2015**, 24, 245.
- [22] M. Yoder, L. Thompson, J. Summers, *Int. J. Solids Struct.* **2018**, 143, 245.
- [23] L. Zhang, B. Song, J. J. Fu, S. S. Wei, L. Yang, C. Z. Yan, H. Li, L. Gao, Y. S. Shi, *J. Manuf. Processes* **2020**, 56, 1166.
- [24] M. Smith, Z. Guan, W. J. Cantwell, *Int. J. Mech. Sci.* **2013**, 67, 28.
- [25] L. Yang, C. Yan, C. Han, P. Chen, S. Yang, Y. Shi, *Int. J. Mech. Sci.* **2018**, 148, 149.
- [26] J. Kadkhodapour, H. Montazerian, A. C. Darabi, A. P. Anaraki, S. M. Ahmadi, A. A. Zadpoor, S. Schmauder, *J. Mech. Behav. Biomed. Mater.* **2015**, 50, 180.
- [27] S. Van Bael, Y. C. Chai, S. Truscillo, M. Moesen, G. Kerckhofs, H. Van Oosterwyck, J. P. Kruth, J. Schrooten, *Acta Biomater.* **2012**, 8, 2824.
- [28] S. Arabnejad, R. Burnett Johnston, J. A. Pura, B. Singh, M. Tanzer, D. Pasini, *Acta Biomater.* **2016**, 30, 345.
- [29] P. F. Egan, V. C. Gonella, M. Engelsperger, S. J. Ferguson, K. Shea, *PLoS One* **2017**, 12, 1.
- [30] H. A. Zaharin, A. M. A. Rani, F. I. Azam, T. L. Ginta, N. Sallih, A. Ahmad, N. A. Yunus, T. Z. A. Zulkifli, *Materials* **2018**, 11, 2402.
- [31] S. P. T. Bhardwaj Singh, M. Shukla, *2017 International Conference on Advances in Mechanical, Industrial, Automation and Management Systems, Allahabad, India, AMIAMS 2017 - Proceedings* **2017**, 333–336, <https://doi.org/10.1109/AMIAMS.2017.8069234>.
- [32] V. Cain, L. Thijs, J. Van Humbeeck, B. Van Hooreweder, R. Knutsen, *Addit. Manuf.* **2015**, 5, 68.
- [33] L. E. Garciandia, *Master's thesis* **2009**.
- [34] G. R. Johnson, *Eng. Fract. Mech.* **1985**, 21, 31.
- [35] T. Mabrouki, F. Girardin, M. Asad, J. F. Rigal, *Int. J. Mach. Tools Manuf.* **2008**, 48, 1187.
- [36] Y. C. Zhang, T. Mabrouki, D. Nelias, Y. D. Gong, *Finite Elem. Anal. Des.* **2011**, 47, 850.
- [37] *ABAQUS User's Manual, version 2016. Dassault Systèmes Simulia Corp* **2015**.
- [38] S. P. Santosa, T. Wierzbicki, A. G. Hanssen, M. Langseth, *Int. J. Impact Eng.* **2000**, 24, 509.
- [39] *13314, I. ISO 13314 Mechanical testing of metals, ductility testing, compression test for porous and cellular metals. Reference number ISO* **2011**, 13314, 1–7.
- [40] M. Mazur, M. Leary, M. McMillan, S. Sun, D. Shidid, M. Brandt, *Laser Additive Manufacturing: Materials, Design, Technologies, and Applications*, Cambridge: Woodhead Publishing, **2017**, pp. 119–161, <https://doi.org/10.1016/B978-0-08-100433-3.00005-1>.
- [41] S. McKown, Y. Shen, W. K. Brookes, C. J. Sutcliffe, W. J. Cantwell, G. S. Langdon, G. N. Nurick, M. D. Theobald, *Int. J. Impact Eng.* **2008**, 35, 795.
- [42] M. Leary, M. Mazur, H. Williams, E. Yang, A. Alghamdi, B. Lozanovski, X. Zhang, D. Shidid, L. Farahbod-Sternahl, G. Witt, I. Kelbassa, P. Choong, M. Qian, M. Brandt, *Mater. Des.* **2018**, 157, 179.
- [43] M. F. Ashby, *Philos. Trans. R. Soc. A* **2006**, 364, 15.

- [44] Y. Li, J. Zhou, P. Pavanram, M. A. Leeftang, L. I. Fockaert, B. Pourn, N. Tümer, K. U. Schröder, J. M. C. Mol, H. Weinans, H. Jahr, A. A. Zadpoor, *Acta Biomaterialia* **2018**, *67*, 378.
- [45] J. Wieding, A. Jonitz, R. Bader, *Materials* **2012**, *5*, 1336.
- [46] S. Limmahakhun, A. Oloyede, K. Sitthiseripratip, Y. Xiao, C. Yan, *Addit. Manuf.* **2017**, *15*, 93.
- [47] C. Öhman, M. Baleani, E. Perilli, E. Dall'Ara, S. Tassani, F. Baruffaldi, M. Viceconti, *J. Biomech.* **2007**, *40*, 2426.
- [48] F. Linde, I. Hvid, *Biomechanics* **1989**, *22*, 485.
- [49] M. F. Ashby, *CES EduPack software*, Granta Design Limited, Cambridge, UK **2019**.
- [50] E. F. Morgan, *J. Biomech.* **2001**, *34*, 569.
- [51] P. Sevilla, C. Aparicio, J. A. Planell, F. J. Gil, *J. Alloys Compd.* **2007**, *439*, 67.
- [52] S. Yang, K. F. Leong, Z. Du, C. K. Chua, *Tissue Eng.* **2001**, *7*, 679.
- [53] C. Öhman, M. Baleani, C. Pani, F. Taddei, M. Alberghini, M. Viceconti, M. Manfrini, *Bone* **2011**, *49*, 769.
- [54] L. J. Gibson, M. F. Ashby, *Cellular Solids: Structure and Properties*, **1997**, Cambridge: Cambridge University Press. <https://doi.org/10.1017/CBO9781139878326>.
- [55] M. F. Ashby, A. G. Evans, N. A. Fleck, L. J. Gibson, J. W. Hutchinson, H. N. G. Wadley *Metal Foams: A Design Guide*, 1st ed., Butterworth-Heinemann, Oxford **2000**, p. 251.
- [56] C. Yan, L. Hao, A. Hussein, P. Young, *J. Mech. Behav. Biomed. Mater.* **2015**, *51*, 61.
- [57] E. Maleki, S. Bagherifard, M. Bandini, M. Guagliano, *Addit. Manuf.* **2021**, *37*, 101619.
- [58] C. Han, Y. Li, Q. Wang, S. Wen, Q. Wei, C. Yan, L. Hao, J. Liu, Y. Shi, *J. Mech. Behav. Biomed. Mater.* **2018**, *80*, 119.